ADVANCED MATERIALS
www.advmat.de

Multifunctionality through Embedding Patterned Nanostructures in High-Performance Composites

*Ozge Kaynan, Ehsan Hosseini, Mohammad Zakertabrizi, Emile Motta De Castro, Lisa M. Pérez, Dorrin Jarrahbashi, and Amir Asadi**

Despite being a pillar of high-performance materials in industry, manufacturing carbon fiber composites with simultaneously enhanced multifunctionality and structural properties has remained elusive due to the lack of practical bottom-up approaches with control over nanoscale interactions. Guided by the droplet's internal currents and amphiphilicity of nanomaterials, herein, a programmable spray coating is introduced for the deposition of multiple nanomaterials with tailorable patterns in composite. It is shown that such patterns regulate the formation of interfaces, damage containment, and electrical-thermal conductivity of the composites, which is absent in conventional manufacturing that primarily rely on incorporating nanomaterials to achieve specific functionalities. Molecular dynamics simulations show that increasing the hydrophilicity of the hybrid nanomaterials, which is synchronous with shifting patterns from disk to ring, improves the interactions between the carbon surfaces and epoxy at the interfaces,manifested in enhanced interlaminar and flexural performance. Transitioning from ring to disk creates a larger interconnected network leading to improved thermal and electrical properties without penalty in mechanical properties. This novel approach introduces a new design , where the mechanical and multifunctional performance is controlled by the shape of the deposited patterns, thus eliminating the trade-off between properties that are considered paradoxical in today's manufacturing of hierarchical composites.

1. Introduction

Directing manufacturing efforts toward the smart methods concentrated on the bottom-up designs from nano and micro features can significantly facilitate the modern material design process. Since the introduction of carbon fibers in the 1950s, and the subsequent onset of carbon fiber reinforced polymer (CFRP) composites, their high strength and stiffness have fueled rapid expansion into aerospace industries, followed by conventional applications such as automotive, portable devices and sports equipment.[1–8] Seven decades of research have been successful in improving and adapting the manufactured CFRP composites for higher machinability, thermal tolerance, and moisture resistance.[9] Despite the continuous progress, a large portion of ongoing research is still focused on mending the weak link in the composite: the interfacial interactions between the carbon fibers and bulk polymer matrix[10–14] and at the mesoscale, the low interlaminar adhesion between neighboring layers (delamination), which have resulted in lower performance than theoretical values in CFRPs.[15] Carbon fibers (CFs)' surface, being chemically inactive and morphologically smooth, provide the little interacting potential for adhesion that is necessary for fast-rate (modulus) and effective (strength) stress transfer from matrix to fiber,[16,17] thus limiting its applications.[18,19]

The conventional approach for mending the two phases together is either to instill higher reactivity in CF by surface treatments,[20,21] to supply the polymer matrix with certain nanofillers,[22,23] and/or to introduce nanomaterials in the form of coating[12,13,24–28] via immersion, grafting or spraying to expand the interfacial region (interphase) and enhance interlocking.[16] The presence of nanoparticles not only increases mechanical bonding through the rough nanoscale morphology of the CF[29] but also provides a larger interacting area for better load transfer between the two phases.[30] Immersion, as the most conventional mode of coating CFs, results in a nonuniform material coverage with improved flexural strength or electrical conductivity.[31,32] While methods such as grafting nanomaterials on the CF improve mechanical properties, the complex fabrication process inhibits its widespread application.[12,33] In addition, the existing

O. Kaynan, A. Asadi
Department of Materials Science and Engineering
Texas A&M University
College Station, TX 77843-3367, USA
E-mail: amir.asadi@tamu.edu
E. Hosseini, M. Zakertabrizi, E. Motta De Castro, D. Jarrahbashi
J. Mike Walker' 66 Department of Mechanical Engineering
Texas A&M University
College Station, TX 77843, USA
L. M. Pérez
High Performance Research Computing
Texas A&M University
MS 3361, College Station, TX 77843-3361, USA
A. Asadi
Department of Engineering Technology and Industrial Distribution
Texas A&M University
College Station, TX 77843-3367, USA

The ORCID identification number(s) for the author(s) of this article can be found under https://doi.org/10.1002/adma.202300948

DOI: 10.1002/adma.202300948

coating methods often require the functionalization of nanomaterials that involve complicated chemical reactions coupled with excessive use of solvents over long processing times.[18,34,35] Additionally, the nearly consistent thickness of the applied layer prevents further engineering microscale patterns of the added nanomaterials and can cause brittleness or slipping of the stacked layers on the interface due to increased stress concentration in agglomerates.[18] As an alternative, spray-coating as a simple and fast method of materials deposition has been used in coating carbon fibers/prepregs with nanomaterials.[36,37] Despite great potential, spraying techniques have only been utilized to mimic dip coating by providing mechanical and interfacial enhancement benefits, albeit with little control over the deposited patterns.[38,39] There is no report on controlling the architecture of embedded nanomaterials, droplet size, associated spray parameters, final deposited patterns and their effect on properties and functionalities of composite. While targeted and precise spraying was shown to be successful in coatings intended for improving electromagnetic shielding,[11] gas separation,[40] and solar cell fabrication,[41,42] it was never combined with capillary flow-driven, hierarchical self-assembly of hybrid nanoparticles to form composites with directed properties. At present, efforts for the self-assembly of materials on desired surfaces are largely limited to surface modifications, guiding templates, or external force, typically via an electric, magnetic, or shear field and non-directed methods.[43] Surface modifications depend on a challenging intense chemical processes[44,45] to attach functional groups to direct the patterns post-evaporation. There have been reports of using external fields, in form of electric,[46] magnetic,[47,48] or shear fields, i.e., applying shear deformation,[49,50] that grant control over particle alignment, yet limited to specific materials and remain questionable in their effectiveness in imposing spatial distribution.[43] Further, prefabricated templates provide a suitable vessel for pattern transfer, however, they are still in their infancy and remain problematic.[51,52] The alternative is engineering the self-assembly through balancing repulsive-attractive-directional interactions within engineered selected set of materials, which besides its simplicity, provides subtle elements for engineering the final pattern.[45,53,54] The addition of controlled order of the nanoparticles without any need for external stimuli or surface modification can be a giant step toward a cutting-edge bottom-up manufacturing technology.

Herein, we introduce an unprecedented bottom-up manufacturing approach, microdroplet coating, in which we fabricate tailorable shaped patterns of nanomaterials in composites to engineer the interactions at lower length scales that determine properties at larger scales. This technique is a step forward compared to conventional methods (e.g., immersion coating) by providing precise control over the extent of coating and the resulting patterns of deposited materials and their associated nanostructures on the substrate. In addition, limitations such as agglomeration, use of multiple materials, and lack of uniform coating of complex or irregularly shaped surfaces will be addressed. In this approach, each engineered-size aqueous droplet consisting of a hybrid nanomaterial system with a specific ratio and concentration creates nanopatterns with desired morphology on the carbon fiber surface after evaporation. The combination of the specific material system (i.e., the amphiphilicity) and droplet size (i.e., the capillary, interfacial, and Marangoni flows inside) engineers the attractive-repulsive-directional forces that determine the assembly of hybrid nanoparticles and form the final deposited pattern. Effective, economic, scalable, and versatile, this novel approach offers a higher level of control over the deposited nanomaterial content and volume to deliver a carefully engineered and homogeneous dispersion and tailorable distribution.

Our method relies on unlocking the potential of tailorable nanoscale interactions applied through the introduction of predetermined patterns on the surface of the CF using hybrid nanomaterials (NMs). These NMs form by fusing the spindle-shaped cellulose nanocrystals (CNCs) with carbon nanotubes (CNTs) and graphene nanoplatelets (GNPs). Previous studies have shown the high colloidal stability in the water created by the presence of abundant –OH groups and negatively charged sulfate half-ester groups on CNCs.[55,56] We aim to eliminate the trade-off between mechanical properties and multifunctionality (i.e., electrical and thermal conductivity) by delivering controllable NMs patterns on CFs through spray coating of CNC-CNT and CNC-GNP hybrid nanoparticles via controlled-size aqueous droplets. Careful consideration was given to analyzing the formations, droplet size, and CNC as the main control factor for patterning, with CNT and GNP as the assembled participants. Deposited patterns with both nanoparticles and prominent CNC content are characterized under SEM micrographs, and their real-time effectiveness in improving the carbon fiber–epoxy interface and interlaminar region is evaluated using short beam shear and in situ bending tests. Complementing the experimental approach, theoretical molecular dynamic (MD) and density functional theory (DFT) calculations are used to explore the underlying mechanisms in the control of self-assembled patterns and their interactions with the composite's surface.

2. Results and Discussion

2.1. Fabricating the Deposited Patterns

Manufacturing engineered sub-microscale deposits are first and foremost, a question of accurate fabrication. This is more challenging in CFRPs as the two phases of CFs and polymer are interacting. In our previous works, we showed the CNC-CNT and CNC-GNP interactions, a unique form of bonding between the defects on the carbon nanoparticles and the charged CNC, responsible for the architecture of the hybrid system that eventually determines patterns ranging between a ring (doughnut) or a disk (uniform thickness).[57,58] In short, the hydrophilic properties of the CNC, lying within the hydroxyl and negatively charged sulfate half-ester groups on its surface, can help disperse and stabilize hydrophobic pristine carbon nanomaterials in aqueous environments.[57] The combination of CNC and carbon nanoparticles creates a unique hybrid system with a specific amphiphilicity that determines the ring or disk patterns after the evaporation of aqueous droplets.[58] Engineering this behavior is enabled by controlling the amphiphilicity of the hybrid nanoparticles system via CNC content and subsequently, the deposited patterns. **Figure 1**a shows the general scheme of the process used to produce and apply hybrid nanoparticles. The hybrid nanoparticles (Figure 1b), formed as a result of bonding between carbon nanoparticles and CNC, are transported with the internal flows of the droplet and deposited in ring or disk formations depending on their

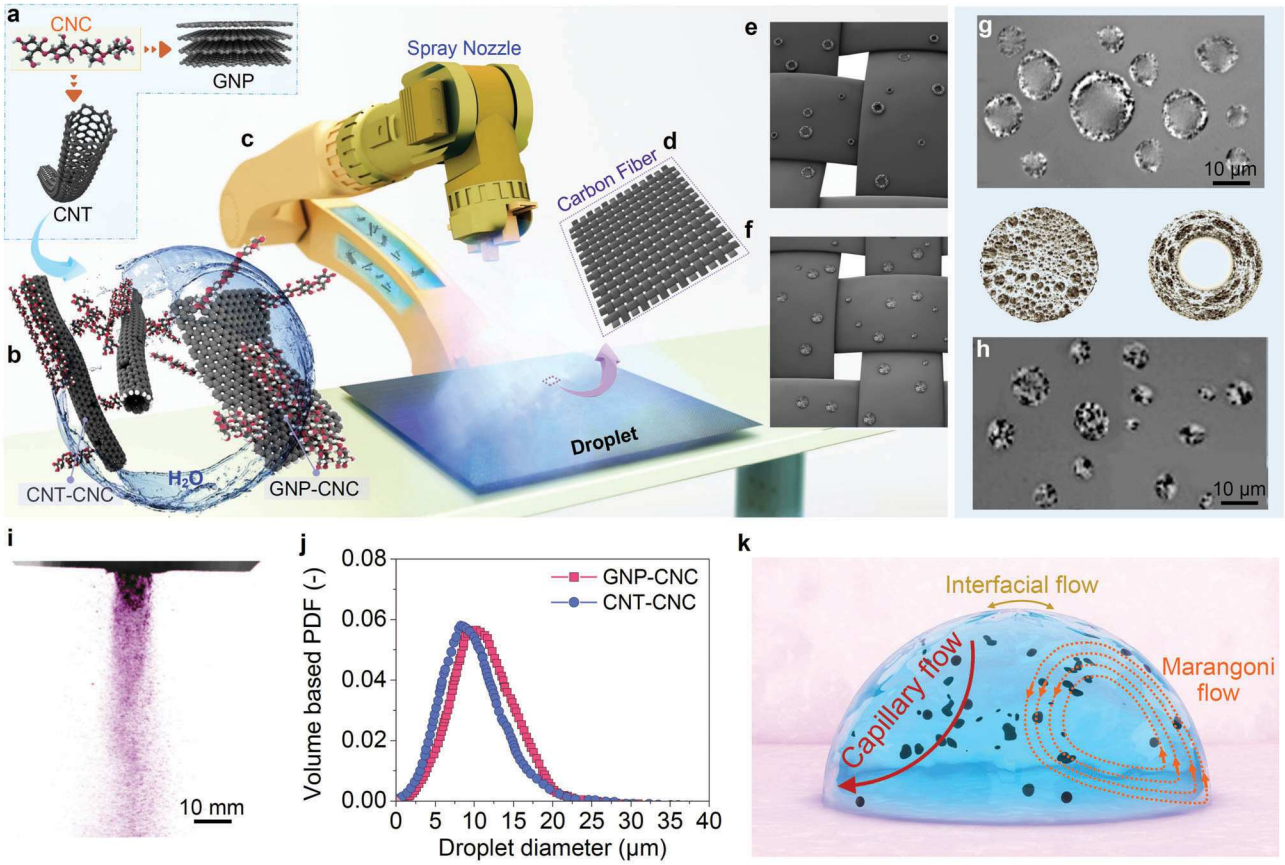

Figure 1. Spray-deposition of nanopatterns: a) CNCs interacting with CNT and GNP, b) dispersed in water, c) being sprayed through a micron size nozzle d) on the carbon fiber surface. Engineered patterns deposited on the carbon fiber: e) ring-shaped and f) disk-shaped patterns. Polarized microscopy images of the g) ring-shaped and h) disk-shaped patterns. i) Spray flow. j) Droplet diameter depicted against the sprayed volume for CNC-GNP and CNC-CNT hybrid nanomaterial systems. The spray and imaging device are shown in Figure S1 (Supporting Information). k) Microflows inside the submicron/nanodroplets.

amphiphilicity. Figure 1c demonstrates a scheme of the working spray depositing droplets on a CF surface using supercritical CO_2 applied within 4 μs time intervals. The droplet size can be controlled from hundreds of nanometers to micrometers (Figure 1j). The result is the surface of the CFs being covered by microscale engineered patterns built with hybrid nanoparticles (CNC-CNT and CNC-GNP), which can range from a ring to disk depending on the predetermined composition of the hybrid nanoparticles architecture in the sprayed suspension (Figure 1e,f). It is noted that both CNT and GNP are pristine with no intended functionalization process. A closer look at the polarized microscopy of these deposits better clarifies their differences in shape (Figure 1g,h). The device responsible for depositing these droplets dispatches a ternary flow (water, CO_2, NMs), complying with the nozzle's specifications (Figure 1i). While the size of the sprayed droplets complies with the size and concentration of the hybrid nanoparticles, the patterns remain within lower microscale, with the majority revolving around 8 μm for CNC-CNT droplets and 10 μm for CNC-GNP droplets (Figure 1j). After deposition on the CF surface, the post-evaporation pattern is formed according to the attractive-repulsive-directional intermolecular forces manifested by capillary, interfacial and Marangoni flows working inside the droplet (Figure 1k).[59,60]

Interacting flows inside the droplet determine the movement and the final positioning of the dispersed particles during and after the evaporation. These forms can affect the interaction between the CF and epoxy interface, which will be further discussed.

2.2. Surface Morphology Evolution

Successful deposition of the ring- and disk-patterned formations is of utmost importance to the manufacturing of our proposed advanced CFRPs. This is observed through a careful review of the morphological features of the modified CF surface. Deposited droplets containing low CNC content (e.g., CNC-CNT 1:4 and CNC-GNP 1:4; *n*:*m* is the mass ratio) dictate a disk-patterned formation, which resembles an array of sub-micron/nano bulges on the surface of the CFs (**Figure 2**a; Figure S2, Supporting Information). On the other hand, droplets containing higher CNC content (e.g., CNC-CNT/GNP 10:1 and 4:1) create ring-patterned formation resembling a doughnut. These formations are guided by modifying the CNC ratio to alter the amphiphilicity of the hybrid nanoparticles. This is supported by the distribution of the oxygen-containing CNC over the nanopattern, shown in the EDS

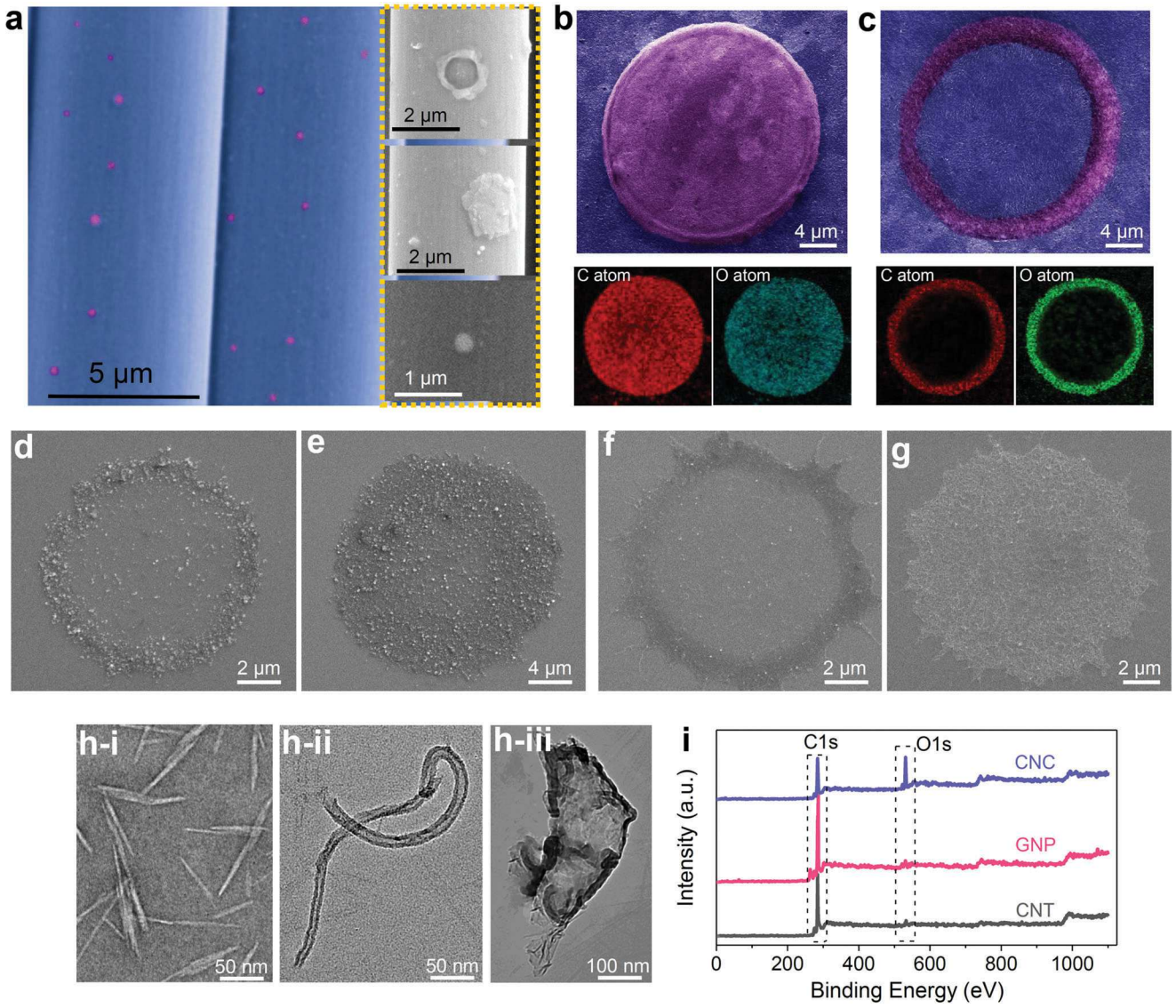

Figure 2. SEM images: a) deposited CNC-GNP droplets on the carbon fiber with high magnification micrographs of ring- and disk-patterned hybrid nanomaterials. b) CNC-GNP 1:4 disk-shaped and c) CNC-GNP 4:1 ring-shaped patterns. CNC-GNP specimen: SEM micrographs of d) CNC-GNP 10:1 ring pattern e) CNC-GNP 1:4 disk pattern. CNC-CNT specimen: f) CNC-CNT 10:1 ring pattern g) CNC-CNT 1:4 disk pattern. TEM images of h–i) CNC h–ii) CNT and h–iii) GNP nanomaterials. i) XPS survey spectra for CNC, CNT, and GNP.

images in the inlet figures, where the presence of oxygen atoms completely overlaps with the carbon atoms from CNT and GNP. In Figure 2a, we present the successful achievement of ring- and disk-patterned nanomaterial architectures on the surface of CFs, with high CNC content (CNC-CNT/GNP 10:1) for the former and low CNC content (CNC-CNT/GNP 1:10) for the latter. More detailed images are brought in Figure 2d–g. The bright spots in Figure 2d,e reflects that the uneven distribution of CNCs on the carbon nanomaterials' surface is influenced by the hybrid nanomaterials system delivered, which has tailored amphiphilicity achieved by the ratio and concentration of the NMs, through size-engineered droplets. As a result, as the water evaporates and patterns emerge, disparities in the surface topology of the pattern become visible as brighter points. These disparities are caused by an uneven stacking process due to the interactions created by the presence of CNCs, in which the side-by-side interaction of the carbon nanomaterials is accompanied by the spatial disturbance caused by covering CNCs. This phenomenon is particularly evident in Figure 2d,e, where CNCs are more noticeable; whereas, Figure 2f,g presents fewer bright points, which means the carbon nanomaterials are more evenly packed together (side-to-side stacking) and less disparity in surface morphology is observed. Overall, these images show the distinctive shapes labeled as disk and ring. Herein, the patterns demonstrated by the CNC-CNT hybrid on the surface of the CF in Figure 2f,g are more pronounced, especially in forming the ring pattern, compared the formations in CNC-GNP deposits (Figure 2d,e). The CNC-CNT hybrid nanoparticles help conserve a more cohesive deposit pattern, which is evident in the formation of a distinct ring pattern. The building components, CNC, CNT, and GNP are demonstrated

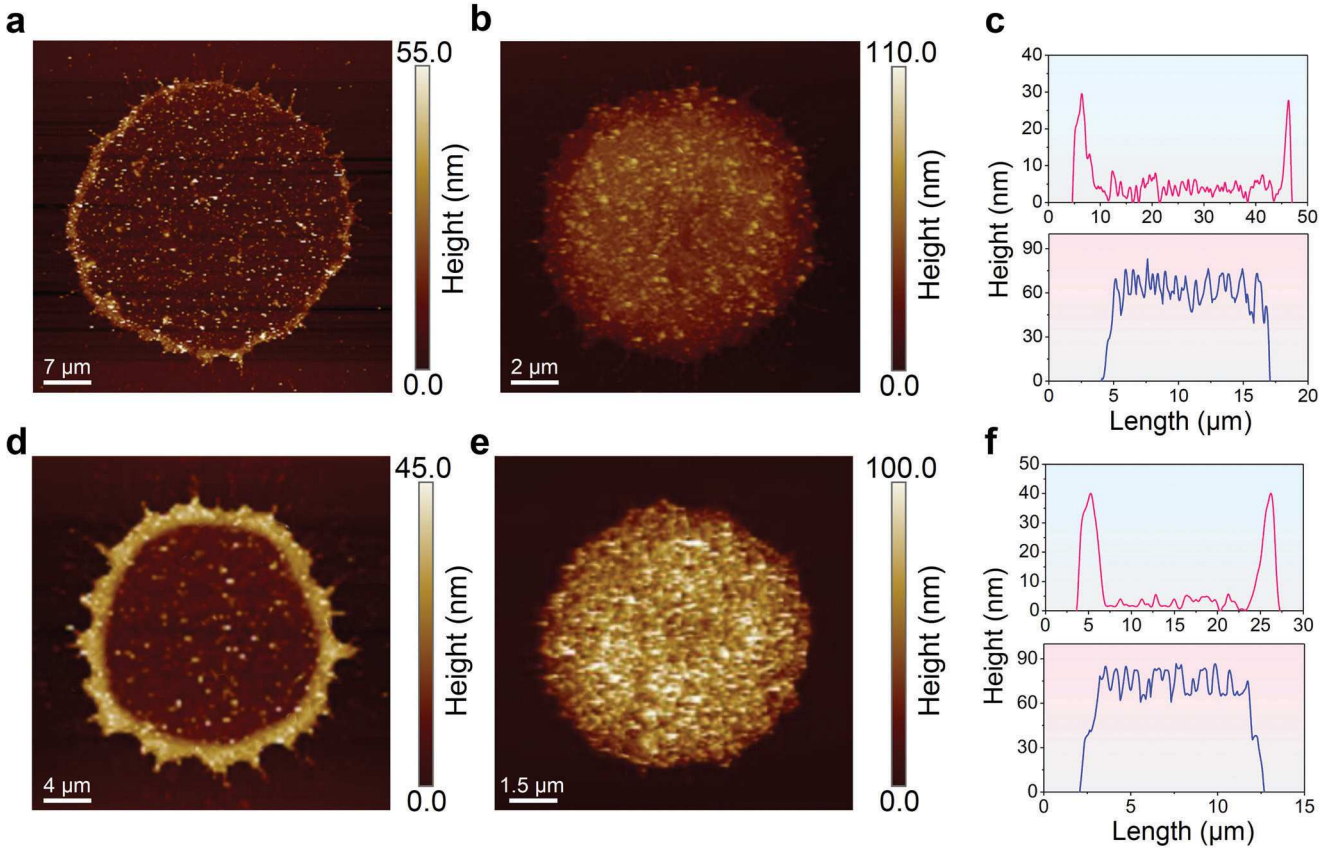

Figure 3. AFM images of CNC-GNP depositions as a) 4:1 ring- and b) 1:4 disk-patterns and the corresponding c) height–length profile of the ring- and disk-patterns formations on the carbon fiber. CNC-CNT deposited as d) 4:1 ring-patterns and e) 1:4 disk-patterns and the corresponding f) height–length profile of the disk- and ring-patterned formations on the carbon fiber.

in TEM imaging in Figure 2h. It can be hypothesized that the cohesive formation of ring/disk-patterned formations in hybrid nanoparticles involving CNT can be attributed to the more flexible morphology of the CNT particles, which are more prone to the droplet's internal flows that dictate the post-evaporation forms. The XPS spectra, shown in Figure 2i, demonstrates the existence of oxygen in the CNC, which is absent or minimal in pristine CNT and GNP. The oxygen content, present in hydroxyl and sulfate groups of CNCs, is essential for interacting with water and interacting with the carbon nanoparticles.

The engineered patterns and the corresponding thicknesses are better shown with a closer look via AFM, where the height of the deposited patterns is marked with a lighter color (**Figure 3**). The CNC-GNP (4:1) ring-patterned formations, shown in Figure 3a, and (1:4) disk in Figure 3b, show a distinguishable dispersion of the hybrid nanoparticles in their corresponding forms. The distribution of the materials is better shown in Figure 3c, where the maximum height of the ring-patterned formation with the particles deposited on the periphery of the formation– reaches 30 nm compared to a near-constant average height of the disk pattern at 80 nm. Similarly, Figure 3d–f depicts the AFM imaging of the 4:1 ring, 1:4 disk, and the height profile of CNC-CNT deposits. Here, similar characteristics are replicated with the maximum height of the particles concentrated on the periphery of the ring-patterned formation reaching 40 nm, compared to the constant height of the disk pattern over the entire surface of the evaporated droplet that stands slightly greater than 80 nm on average. Comparing corresponding ring- and disk-patterned formations, disk patterns show larger height, ≈2–3 times the height of the ring-patterned formations. The ring-patterned CNC-CNT formation, shown in Figure 3d, has a greater maximum height at 40 nm, ≈33% higher than the corresponding ring-patterned CNC-GNP formation. However, deposits comprising disk-patterned formations show similar average height at 80 nm, with CNC-CNT standing slightly (<8%) higher (Figure 3e,f). These profiles reflect a nanoscale height for both ring- and disk-patterned formations, whose magnitude can be further controlled through concentration and spray time.

The AFM images resemble the height profiles in Figure 3c,f, confirming the existence of the disk- and ring-patterned formations, both of which enhance the interacting surface of the carbon fiber. With the inner and outer wall morphology of the rings, the ring-patterned formations can be expected to have a higher engagement with epoxy, further enhancing the mechanical interlocking and physiochemical interactions at the interfaces of the two phases of the composite. Each of these patterns can tailor the microscale interactions between the carbon fiber and infused polymer that determine the microstructure and engineer the mechanical and functional properties, as discussed below.

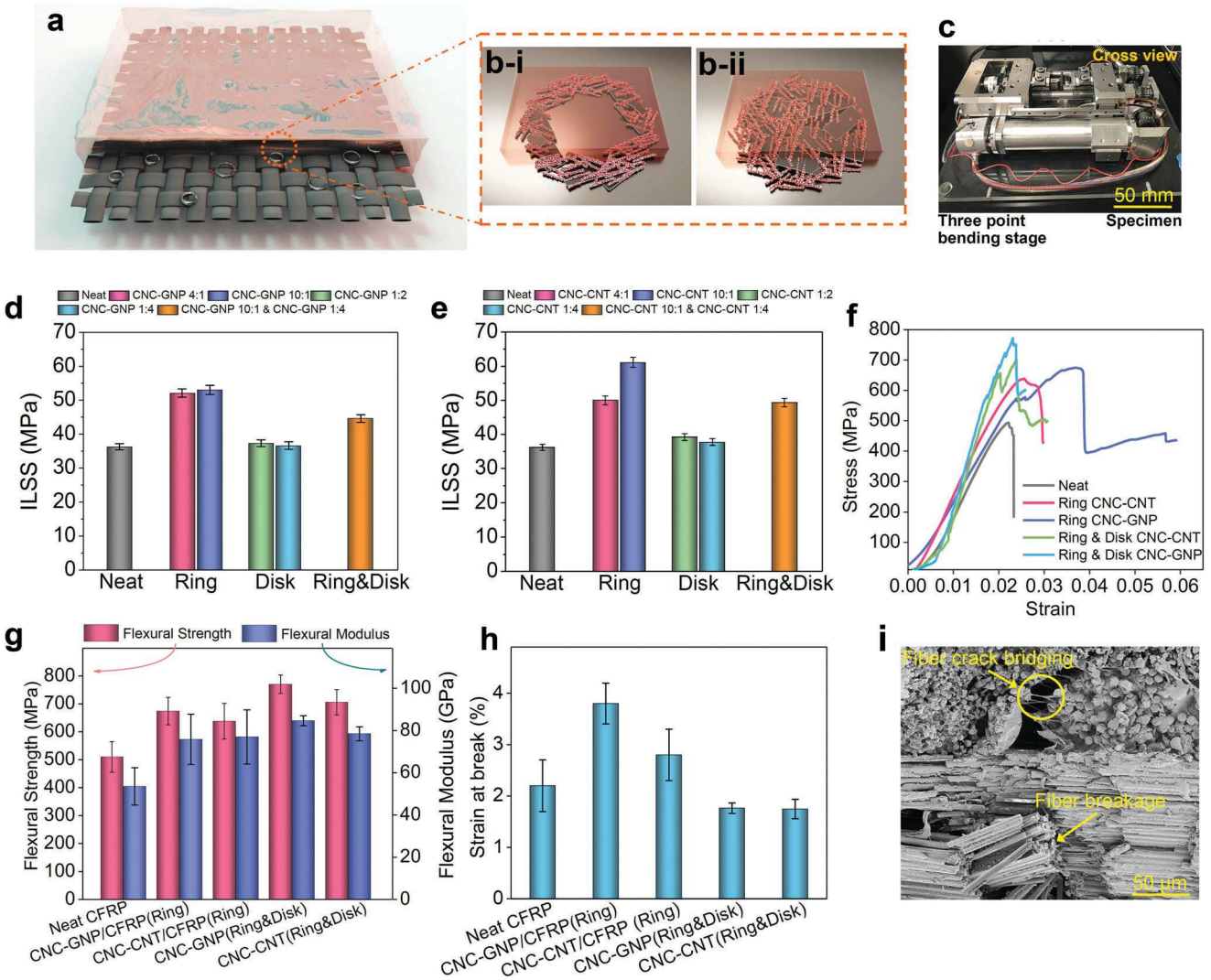

Figure 4. Sprayed carbon fiber-epoxy resin structure: a) hybrid nanomaterials deposits on the composite, a closer look: b-i) resin-covered ring pattern and b-ii) resin-covered disk pattern. c) Three-point bending stage used for in-situ flexural tests. ILSS test results: d) CNC-GNP, and e) CNC-CNT with the ring-patterned CNC-CNT/GNP, disk-patterned CNC-CNT/GNP, and ring- and disk-patterned CNC-CNT/GNP CFRPs. In-situ bending results: f) Representative stress-strain diagram, g) flexural strength and modulus, and h) strain at break of neat, ring-patterned CNC-CNT/GNP, and the ring- and disk-patterned CNC-CNT/GNP sprayed CFRP. SEM image of post–fractured surfaces of the short beam test samples t: i) ring-patterned 10:1 CNC-CNT sprayed CFRPs. The scale bar is 50 µm.

2.3. Tailorable Mechanical and Multifunctional Properties of Spray-Deposited Carbon Fiber Reinforced Polymers

The cohesion in the interfacial region between CF and epoxy governs the mechanical and multifunctional (electrical and thermal) properties of the composite. Therefore, the introduction of sprayed patterns to this region directly influences the cohesion through surface interactions, whose composition depends on the deposited patterns shapes applied by modifying the ratio of CNC-CNT/GNP. The deposited patterns are situated in the interface region between the epoxy and the fibers, mediating the interactions between the two as shown in **Figure 4**a. Different patterns, ranging between ring (Figure 4b-i) and disk (Figure 4b-ii), help mediate the cohesion in the interfacial and interlaminar (interlayer) regions, the effects of which can be observed in results from the interfacial shear strength (IFSS, Figure S3 Supporting Information) and interlaminar shear strength (ILSS, Figure 4d,e) evaluated by short beam shear (SBS) test (Figure 4c). The inclusion of individual CNC, GNP, and CNT proved to have little effect on the ILSS and tensile results (Figure S4, Supporting Information). For the CNC-GNP–CFRP, the ring-patterned formations show 48% higher ILSS (≈52 MPa) than the neat CFRPs (≈36 MPa). In contrast, applying disk-patterned formations results in decreasing the interlaminar strength on par with the neat CFRP. A closer look reveals that changing CNC-NM ratios from 1:2 to 1:4 without disturbing the distinct form of a disk, or from 4:1 to 10:1 without altering the ring-patterned formations, does not culminate in a meaningful change in the ILSS. The results are similar for CNC-CNT composition, with one caveat: increasing the CNC content, i.e., transitioning from disk- to

ring-patterned formations, is accompanied by a further increase in the interlaminar strength. Depositing CNC-CNT disk patterns on CF returns the same results as the CNC-GNP patterns, at nearly 36 MPa. However, the specimens with ring-patterned formations climb to ≈50 and ≈60 MPa (66% increase compared to neat's) in ILSS of the 4:1 and 10:1 CNC-CNT–CFRP, respectively. Furthermore, alternating ring- and disk-patterned formations (manufacturing details can be found in Figure S5, Supporting Information) result in slightly lower ILSS values compared to that of ring-patterned CNC-CNT/GNP with 44 and 49 MPa for CNC-GNP and CNC-CNT, respectively. This indicates that ring-patterned formations presence dominates the fiber–matrix interface through the internal cohesion with epoxy molecules. The greater enhancement of the IFSS (Figure S3, Supporting Information) of ring-patterned CFRPs (65% larger than neat's) compared to disk-patterned (no significant change) and ring- and disk-patterned (47% larger than neat's) also confirms a stronger fiber-matrix adhesion in the ring-patterned composites. These results show that ring-patterned hybrid nanomaterials (NMs) deposition result in enhanced interfacial and interlaminar mechanical properties in CNC-GNP– and CNC-CNT–CFRPs.

The effect of sprayed ring-patterned formations of NMs on the mechanical properties of CFRPs was further evaluated by in situ flexural tests in a three-point bending stage under an optical microscope. In situ bending testing is an effective way to observe the real-time flexural deformation of the samples under a combination of transverse tensile and in-plane shear loads.[61] For flexural tests, only champion samples of ILSS, i.e., ring-patterned formation of CNC-CNT 10:1 CNC-GNP 4:1, and the ring- and disk-patterned of CNC-CNT/GNP were used. Figure 4f shows the representative force-displacement curves of neat and spray-coated ring-patterned and ring- and disk-patterned of CNC-CNT– and CNC-GNP–CFRP composites under a three-point bending test. The neat specimen breaks (or delaminates) catastrophically, while the spray-coated specimens show a clear post-break strength. This is highlighted in the stress-strain curves, where neat specimens exhibit a linear elastic regime followed by a stress drop, while patterned CFRPs exhibit non-linear behavior suggesting progressive damage and change of failure modes compared to neat CFRPs. In the elastic regime, the slopes of stress-strain curves of CNC-CNT– and CNC-GNP–CFRP are greater than that of the neat composites in Figure 4f, which implies that all reinforced composites exhibit greater modulus than that of neat. Ring-patterned CNC-CNT– and CNC-GNP sprayed CFRPs resist delamination at 630 and 660 MPa with 0.03 and 0.04 strain at break, respectively, compared to that of neat CFRP with 490 MPa, whereas the ring- and disk-patterned CNC-CNT and CNC- GNP sprayed CFRPs present the strength of 700 and 770 MPa with a tradeoff in strain at break (0.02) as indicated in Figure 4f. This indicates that ring-patterned CNC-CNT and CNC-GNP on CF surfaces strengthen both the fiber–matrix interface and adhesion between neighboring layers, thus enhancing the delamination resistance and crack retardation of composites.

The statistically calculated flexural modulus, flexural strength, and flexural strain at break are summarized in Figure 4g,h. Spray-coated ring-patterned CNC-GNP and CNC-CNT increase both flexural modulus by 40% and 41% and flexural strength by 33% and 25% compared to those of neat samples, respectively. Due to the highly cross-linked structure of thermoset composites, reinforcing them with nanomaterials boosts their strength and modulus with a trade-off strain at break.[28,62] However, in CNC-GNP–CFRP and CNC-CNT–CFRP, in addition to flexural strength and modulus, the strain at break is enhanced by 32% and 73%, respectively. This improvement, which is disruptive to literature, is attributed to fiber-matrix enhancement through the synergetic effect of CNC and CNT/GNP, owing to CNC's oxygen-containing functional groups for better chemical bonding (formation of covalent bonding between –OH and half ester sulfate groups of CNC and the defected sites of CNT/GNP during the ultrasonic treatment[57]) and CNT/GNP's stiff wrinkle structures for mechanical interlocking leading to strong particle–matrix and matrix–fiber interfaces.[63] According to the interfacial shear strength (IFSS) results in Figure S3 (Supporting Information), ring-patterned CNC-CNT (10:1 ratio) enhances IFSS by 75% compared to that of neat composite, which confirms the fiber-matrix enhancement. More detailed micrographs and the corresponding details on the flexural stress-strain curves are brought in Figure S6 (Supporting Information) and the interfacial properties of neat, ring, and disk CNC-CNT/GNP sprayed CFRPs represented by IFSS are shown in Figure S3 (Supporting Information).

The ring- and disk-patterned CNC-CNT and CNC-GNP sprayed CFRPs exhibit the highest flexural strength (705 and 770 MPa, respectively) and modulus (78 and 84 MPa, respectively) higher than both neat and solely ring-patterned composites (Figure 4g). However, there is a trade-off as evidenced by the decreased strain at break presented in Figure 4h. The higher loading of NM in the disk regions of the composites increases the composite stiffness locally; however, this limits the load transfer across the disk features due to the ineffective cohesion to the epoxy compared to ring patterns. The IFSS results in Figure S3 (Supporting Information), also confirm that the adhesion of the fiber–matrix interface in the ratios that create rings is stronger compared to those that form disks, suggesting a higher capability of load transfer of ring-patterned composites. While the ring pattern provides more efficient load transfer, the uniform distribution of high-stiffness NMs in the disk patterns provides a higher rate of stress transfer and dissipates more energy in failure by unbundling CNT/GNP entanglements. By combining these two strengthening methods, the tensile/compressional response – showcased in flexural properties – of the combined patterns can exceed the strength of the sole ring or disk with the primary drawback of lower strain to failure.

Figure 4i represents the post-fracture SEM images of CNC-CNT sprayed CFRPs tested in three-point bending. Compared to the smooth fracture surfaces and fibers devoid of the matrix in the neat composite (see Figure S7, Supporting Information), rugged surfaces indicate interfacial interlocking, and zigzagged matrix cracking with micron-level bridges implies crack arrest, enhanced interfacial interactions, and multi-modal fracture. These mechanisms cooperatively retard the delamination to a ≈150 MPa higher stress level compared to neat composites. In addition, we have shown that amplified physio–chemical interactions at the interface via oxygen-containing functional groups of CNCs extend the interfacial region (interphase) to the depths of polymer matrix and enhance the interfacial stiffness and strength leading to faster and more efficient stress transfer across fiber

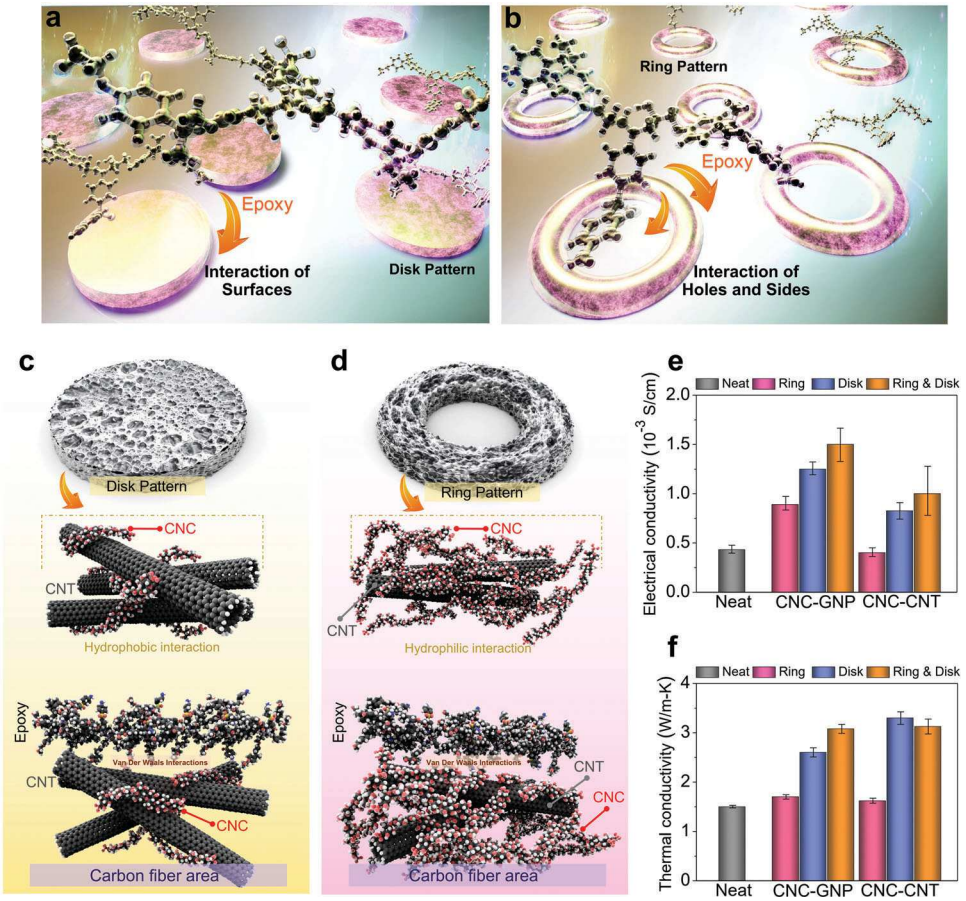

Figure 5. The spatial form of CNC-NM patterns affects intermediating interactions within epoxy-CF interface in a) Disk b) Ring formations. Increasing CNC content from c) disk- to d) ring-patterned formations shift the unmediated interactions within NM stacks to CNC-mediated interactions. The macroscale effects of the change are apparent in e) electrical and f) thermal conductivity of hybric nanomaterial deposited CFRPs.

and matrix. More details on the post-mortem three-point bending specimens are brought in Figure S7 (Supporting Information).

The tailorable effect of the sprayed patterns in the interfacial region is governed by their form and composition, both of which significantly influence the binding interactions between the CF and epoxy via nanopattern intermediation. This is depicted in **Figure 5**, with the effects of shape and composition distinguished in Figure 5a–d. The disk pattern provides a single smooth surface for interaction with the epoxy molecules, whereas the ring pattern provides an additional surface from the inner ring wall that further solidifies the epoxy-CF interfacial cohesion. It can be hypothesized that the additional interacting surface in the ring pattern compared to the disk pattern provides additional surface coupling to achieve the high mechanical performance observed in Figure 4. In other words, the interacting surfaces in and outside the ring pattern play a significant role in epoxy-CF entanglement at the atomic scale. Furthermore, since the effective distribution of stress depends on strong interactions between both phases of the composite, the presence of a third phase in form of deposited nanopatterns in the interface means load transfer also depends on the internal cohesion of the nanopatterns. Therefore, the presence of nanopatterns without sufficiently strong internal cohesion can create sites that cause unexpected forms of deformation and induce premature failure of the composite regardless of the nanopattern-epoxy or nanopattern-CF interactions. MD simulations followed the strength of interactions within the nanopatterns in both forms through radial distribution function (RDF) values, which represent the post-evaporation order within the nanopattern. Stronger interactions between the components are reflected in a more ordered formation, which correlates with the higher share of CNC particles (Figures S8 and S9, Supporting Information). In addition, CNC particles were found to be indispensable in reducing the presence of unmediated stacks of NMs, which were shown to be a possible weak link in stress transfer. This means that due to the differences in the stacking forms, the internal cohesion of the disk-patterned formations, with a larger share of unmediated NM–NM, is weaker than their ring-patterned counterparts, which results in easier slipping and separation in the pattern itself under stress (see Figure S10, Supporting Information). The CNC-mediated interactions in the post-evaporation stacking formation exert a form of internal order, whereby CNC particles increasingly penetrate the space between NMs and replace the unmediated NM–NM interactions with NM-CNC-NM interactions. Since the presence of CNC particles is a part of the hybrid system designed to provide a stable dispersion, their role in shaping the post-evaporation stacking form is

universal and nanomaterial-agnostic. More details are brought in Figures S8–S14 (Supporting Information). The observed enhancement to the internal cohesion of the third phase (deposited nanopatterns) as a result of added CNCs means more effective load transfer in the interface region.

Controlling the shape of the pattern through engineering its composition is the key to regulating this mechanism, where additional interactive surfaces can be added or subtracted at the submicron scale. The chemical composition of the sprayed droplets comes into effect when conductive carbon nanomaterials form deposits intertwined with isolating CNC species. Increasing the share of carbon nanomaterials while keeping the suspension concentration constant, i.e., transitioning from ring to the disk pattern, diminishes the contact between adjacent carbon nanomaterials and thus shrinks the conductive network (Figure 5a–d). Given the scale of GNPs compared to CNTs, CNC-GNP patterns provide better vessels for electrical/thermal conductivity due to their larger size that creates a larger connected conductive network by contact. In contrast, CNTs are more likely to be misoriented, or coated with CNC or epoxy, hindering the advantage in out-of-plane electrical conductivity. The result is a tailorable electrical conductivity, which can be paired with the mechanical benefits discussed above, that is solely dependent on the shape of the patterns detailed in Figure 5c,d. While the ring pattern in CNC-CNT provides the same level of electrical conductivity as the neat specimen, the disk pattern shows twice higher electrical conductivity at 0.88×10^{-3} S cm^{-1}, which is on par with the ring pattern in the CNC-GNP specimen (Figure 5e). The electrical conductivity of 1.26×10^{-3} S cm^{-1} in CNC-GNP disk-patterned specimens is three times higher than in neat specimens. The highest electrical conductivities are achieved in the combined ring- and disk-patterned CNC-CNT/GNP composites, with CNC-GNP reaching up to 1.52×10^{-3} S cm^{-1}. Conductive networks can be formed through direct contact, or by proximity through tunneling.[64] CNC in the ring structures limits the entanglement of NMs to effectively space NMs and create a tunneling electrical network. In the disk patterns, the low CNC quantities will increase the probability of CF/CNT/GNP interactions to occur, which significantly benefits the conductivity pathway via direct contact. Combining the two patterns effectively creates two separate conductive pathways, resulting in the highest observed electrical conductivity with the combined ring and disk.

The thermal conductivity follows the same trend in terms of ring and disk patterns; however, CNC-CNT shows greater conductivity than CNC-GNP, shown in Figure 5f. Here, the thermal conductivity of the CNC-CNT ring patterns was measured around 1.5 W m^{-1} K^{-1}, similar to that of the neat specimen. Transitioning to the disk pattern significantly increases the conductivity by 117% to 3.25 W m^{-1} K^{-1}, going above the thermal conductivity values for both ring and disk in CNC-GNP specimens. The differences are less pronounced in CNC-GNP specimens, where the disk pattern shows a thermal conductivity of 2.55 W m^{-1} K^{-1} over the 1.68 W m^{-1} K^{-1} of the ring pattern. Furthermore, thermal conductivity of combined ring- and disk-patterned CNC-CNT and CNC-GNP reaches the CNC-CNT/GNP disk-patterned composites at 3.1 W m^{-1} K^{-1}. Figures 4 and 5, and Figure S4 (Supporting Information) indicate simultaneously enhanced mechanical (ILSS and flexural strength) and conductive (electrical and thermal) properties in combined ring- and disk-patterned CNC-CNT/GNPCFRP composites. The mechanical properties are maximized by the CNC loading in the ring patterns as CNC serves as a surface compatibilizer between the chemically inert CNT/GNP and epoxy. For the thermo-electrical functionality, we observe conductivity matching disk results as the localized higher CNT/GNP loadings improve the through-thickness conductivity of the composites. This suggests that combining various nanomaterial patterns allows engineering the multi-functionality of the CFRP composites with no penalty on structural properties.

2.4. MD Simulations

The functionality-structural benefits abide in the integration of the nanopattern within the epoxy-CF composite through intermolecular forces that guarantee cohesion in the interface. The interactions between the nanoparticles and CNC are discussed at length in (Figures S11–S15, Supporting Information). Here we use MD to understand the effect of the CNC-GNP/CNT ratio on the bonding energies between different species. This translates into the chemical stability of the self-assembled nanostructures at higher scales in the composite. The molecular configuration at the surface of the CF is shown in **Figure 6**a, where the CNT interacts directly with CF and indirectly– through the CNC cover– with the epoxy. Two configurations of CF-CNT1/CNC2/epoxy (CNC content is twice of CNT) and CF-CNT2/CNC1/epoxy (CNT content is twice of CNC's) are modeled to determine the bonding energies, as shown in Figure 6b. The binding energy value in CF-epoxy and CF-CNC pairs have similar values, at nearly −30 kJ mol^{-1} nm^{-2}. In comparison, the bonding energy values in CF-CNT1/CNC2/epoxy and CF-CNT2/CNC1/epoxy show higher values at −40 and −45 kJ mol^{-1} nm^{-2}, respectively. These numbers demonstrate a stronger interaction between the CF and CNT/CNC/epoxy compound (sprayed surface) compared to the original interaction between CF and epoxy in the neat composite, which translates into an efficient load transfer and higher tolerance against crack propagation in the sprayed spots where the nanopatterns form.

The interactions residing within the nanoscale deposits and the two phases of the composite depend on the positioning of the nanoparticles, which itself rests on the sufficient presence of CNC. Therefore, while increasing the presence of nanomaterials may help reinforce the cohesion in the interlayer, we still require balancing the specific reactive surface according to the presence of the nanomaterials and their positions. In the ring pattern, the higher presence of CNC provides a higher specific surface for the nanomaterials to form more effective bonds between the two phases. Since the dispersion factor and possible crack paths cannot be traced in the MD simulations, the bonding tendencies at the molecular level should be considered separately. Considering a possible range of stable CNC-CNT dispersions, the simulation results show that the synergistic effect of CNC and CNT can improve the bonding between the two phases of the composite based on the optimum ratio for the desired application.

The results for the CNC-GNP sprayed composite are similar, as depicted in Figure 6b. While the interactions between CF and the nanopattern show the highest bonding energy, it is the CNC/GNP/epoxy compound, covering the surface of the CF that forms the interfacial weak link. The internal cohesion

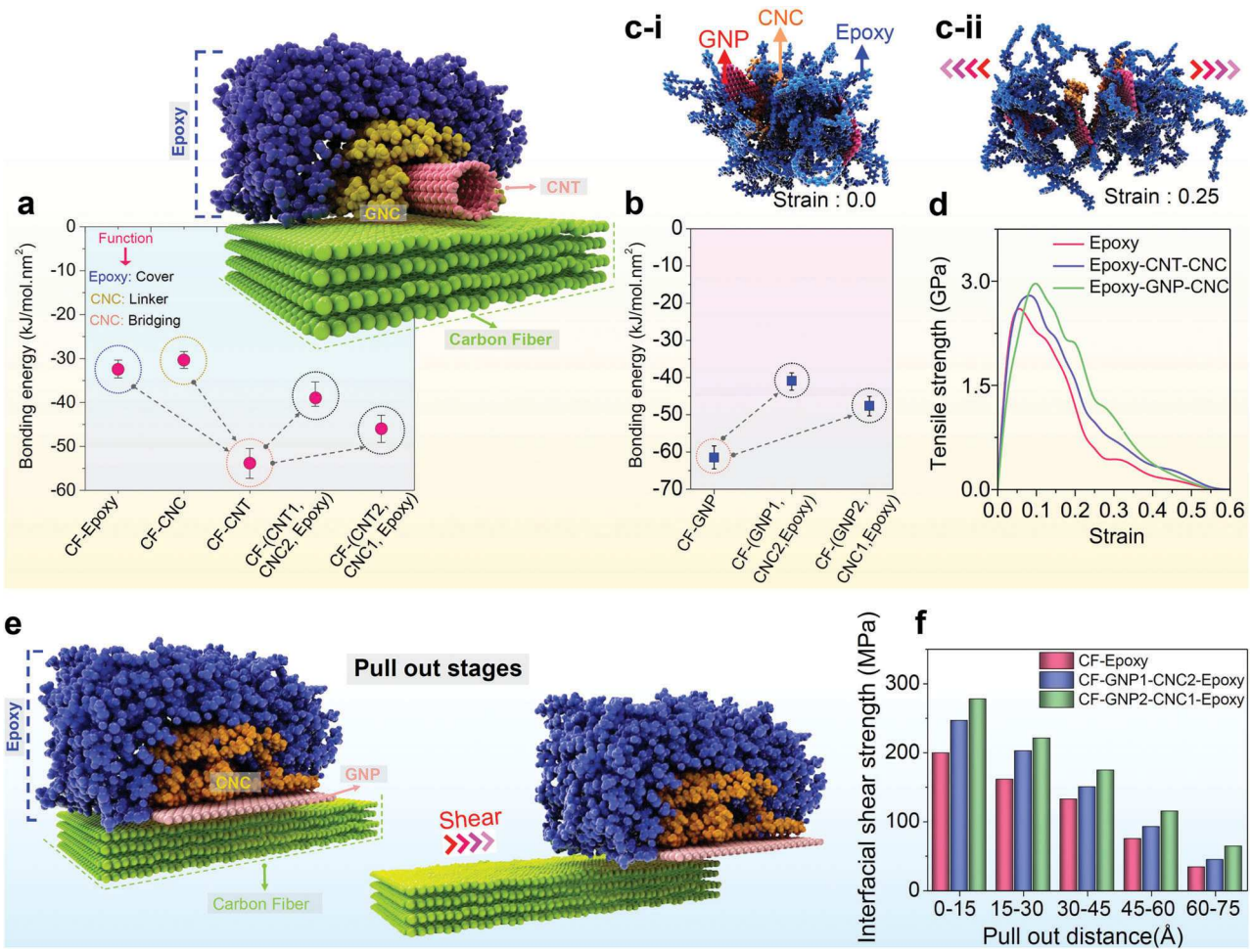

Figure 6. Bonding energy between different pairs on the surface of the a) CNC-CNT, and b) CNC-GNP sprayed CF plate. c) The internal cohesion of GNP-CNC-epoxy under strain. d) Tensile strength of the sprayed epoxy compound. e) The sliding process of sprayed CF in the presence of CNC-GNP and epoxy is represented by: f) Interfacial shear strength of the sprayed patterns on the CF surface.

of this compound is evaluated through directly enforced strain, schematically shown in Figure 6c. The results paint a comparatively similar picture in Figure 6d, albeit with higher strength values demonstrated by the CNC-GNP and CNC-CNT, respectively. This means the inclusion of the nanopatterns within the epoxy–CF interface as an intermediary not only strengthens the overall adhesion between the two main phases but also improves the internal cohesion of the epoxy. Increasing the share of CNC particles in the droplets results in replacing the unmediated NM–NM interactions with NM-CNC-NM interactions (see Figures S8 and S9, Supporting Information), the effects of which at the molecular level are explored in Figure S10 (Supporting Information).

The efficacy of the deposited CNC-CNT/GNP in bonding the two main phases is better demonstrated through sliding evaluation, whereby the NM-CNC-epoxy nanopattern is pulled on the surface of the CF, as depicted in Figure 6e. The results, brought in Figure 6f, show the improved mediated adhesion between CF and epoxy. This adhesion is represented by interfacial shear strength. The interfacial shear strength for CF-epoxy peaks at 200 MPa with less than 15 Å displacement, and slowly declines until it reaches 38 MPa at 75 Å displacement. The corresponding values for the epoxy CNC-GNP deposits are 283 MPa at 15 Å and 62 MPa at 75, respectively. These numbers show an astounding improvement, over 40%, which can be translated to the considerable role of the CNC-CNT and CNC-GNP deposits in intermediating the stress transfer between CF and the epoxy matrix, and their plausible role in deflecting and hindering cracks.

3. Conclusion

We explored the theoretical and experimental aspects of introducing submicron ring and disk-patterned deposits into the interface of carbon fiber and polymer to engineer the structural and multifunctional performance. We present a new bottom-up approach, based on controlling the spray-deposited patterns of the self-assembled hybrid nanomaterials (i.e., CNC-CNT and CNC-GNP assemblies), whose shapes vary from complete rings to disks over the carbon fiber surface with decreasing CNC mass ratio. The insertion of these patterns composed of hybrid nanomaterials on the carbon fiber surface adds patterned nanostructures and topology that alters the interacting surfaces of carbon fiber and epoxy. Although both ring and disk patterns enhance the

ILSS and flexural stiffness and strength by arresting cracks, disturbing their path, and altering fracture modes, ring patterns result in higher ILSS and flexural properties compared to disk patterns. This is mainly due to the inner and outer surfaces of rings that act as double-interacting surfaces resulting in higher interfacial interactions. In comparison to the disk-patterned formations, the ring-patterned formations of CNC-CNT and CNC-GNP enhance the ILSS by up to 67% and flexural strength and strain at the break by up to 36% and 73%, respectively due to the synergetic effect of hybrid CNC-CNT/GNP. The multifunctionality of ring and disk patterns is reflected in the electrical and thermal conductivity of the composites. The disk patterns show higher electrical and thermal conductivity compared to ring patterns for both CNC-CNT and CNC-GNP. While CNC-GNP specimens show the highest electrical conductivity (nearly three times the neat specimen), the CNC-CNT specimens performed better in thermal conductivity, showing ≈2.3 times the thermal conductivity of the neat specimen. When ring and disk patterns are combined, the resulting composites show greater overall mechanical and functional properties than the individual patterns, with 62% higher flexural strength and 280% and 93% larger electrical and thermal conductivity compared to neat CFRPs. The mechanical properties of the combined ring- and disk-patterned CFRP adopt the improved interface and load transfer capabilities of high CNC loadings found in ring patterns, whereas the functional properties demonstrate improvements representative of both ring and disk by development of a structured tunneling pathway (ring), and a direct contact pathway (disk) for conductivity. This study demonstrates that combined usage of both patterns can concurrently maximize structural and multifunctional properties without sacrificing one for another.

To further explore the underlying factors, we used advanced MD and DFT techniques to dissect the precise intermolecular forces lying within the CNC-CNT(GNP)–CF/epoxy composite interface. The results show that increasing the CNC content is synonymous with rising sliding resistance (interfacial shear strength) and cohesion within the interface. The phase binding in the new CNC-GNP/CNT surface morphology benefits from the relatively higher affinities between CNC content, CF surface, and the CNT/GNP. Most importantly, the presence of nanomaterials plays a key role in improving the internal cohesion of the epoxy phase and creates strong localized interactions between carbon fiber and epoxy-nanopatterns. These interactions create resilient points to divert cracks and introduce functionality in the form of improved conductivity. This study demonstrates the successful implementation of a highly tailored and scalable method for engineering the microstructure of hierarchical materials on the nanoscale with pre-determined patterns. The proposed approach advances the ultimate goal of tailoring composites from the nanoscale one step further by achieving mechanical performance and multifunctionality through the lens of precise, high-throughput manufacturing.

4. Experimental Section

Materials: Commercially available unidirectional Hexcel IM7 Intermediate Modulus CFs were used as received in this work. Epoxy INF-114 and INF-211 hardeners were supplied from Pro Set, USA. NCV-100 CNCs (CelluForce, QC, Canada) with a diameter of 2.3-4.5 nm and length of 44–108 nm were used as received. The pristine multi-walled CNTs purchased from USNano (USA) were produced via catalytic CVD with 95% carbon purity with an average outer and inner diameter of 5–15 and 3–5 nm respectively, length of 50 µm, and wall count of 12 with 1.62 Å spacing. Wall spacing was measured by transmission electron microscopy (TEM).

Spray System: The nanomaterials were integrated by using a custom-made spray system manufactured in the facilities. CNCs and CNC-CNTs were sprayed onto unidirectional CF fabrics as per the conditions given in Figure 1. Six different coating suspensions: CNC-GNP 1:4, CNC-GNP 4:1, CNC-GNP 10:1, CNC-CNT 1:4, CNC-CNT 4:1, CNC-CNT 10:1 were prepared, each with a total 0.4 wt.% concentration. CNCs were dispersed in 500 mL of deionized water (DI-H2O) using probe sonication (Qsonica Q125 equipped with a sonotrode of 6 mm) for 3 h at a frequency of 20 kHz and 75% intensity in an ice bath. For CNC-CNT suspensions, CNTs were dispersed in pre-sonicated, aqueous CNC suspensions under the same sonication conditions for 3 h. At this stage, the specimens with higher CNC content (i.e., CNC-CNT/GNP 4:1, CNC-CNT/GNP 10:1) showed ring-patterned formations after evaporation, in contrast to the disk-patterned formation left after the evaporation of water from specimens with lower CNC content (i.e., CNC-GNP/CNT 1:4). The suspensions were poured in the 80 mL volumetric capacity spray gun to deposit the CNC-GNP/CNT onto both sides of the CF fabric (304 × 304 mm,) at room temperature. After the coating process, the CFs were dried at room temperature overnight followed by drying in an oven (Across International AT09) at 120 °C for a day. The drying time is determined based on the thermogravimetric analysis (TGA) confirming that there is no water on CF. Ten layers of the spray-coated CF fabrics were then cut into 152 × 152 mm squares and used for manufacturing the composite laminates.

The droplet size was controlled by the spray parameters such as gas-to-liquid mass flow rate ratio (GLR), injection pressure (7.5 MPa), nozzle diameter (125 µm), and axial distance from the injection nozzle (15 cm), and these parameters were used throughout this current study. The detailed characterization of the droplets can be found in the previous words.[65]

Fabrication of Spray-Coated CNC and CNC-CNT Laminates: The hybrid composites were manufactured using ten spray-coated CF layers with $[0,90,0,90,0]_s$ stacking sequence by vacuum-assisted resin transfer molding (VaRTM) process. The CF layers were stacked and placed over a Mylar sheet on the surface of a 450 × 450 mm rectangular mold, which had an adhesive silicone heater right in the middle of the mold plate. A peel ply layer was added on the top of the CF layers to prevent sticking, and pieces of infusion mesh were placed at the top to promote resin flow. The entire package was enclosed in a vacuum bag and sealed with two-sided butyl tape. Two external hoses were connected to the inlet of the resin and vent to the vacuum pump. Before resin infusion, the inlet was closed, and the vacuum pump was then turned on to draw the air trapped inside the mold. After establishing the vacuum, the degassed resin was infused from the inlet. The excess resin was removed from the vent, the inlet was closed, and the vent was then left open for 8 h until the resin was cured. Flexural, interlaminar shear stress (ILSS), and in situ bending samples were cut from the fabricated plates using a computer numerically controlled router (Mill Right).

Characterization Techniques: Scanning Electron Microscopy (SEM) was used to visualize the quality of the CNC and CNC-CNT spray-coated surface, and the fractured surface of the tested samples. Tescan FERA-3 Model GMH Focused Ion Beam Microscope with an acceleration of 10 kV was used.

A short beam shear test (SBS) was performed to reveal the ILSS of neat and coated CFRP according to ASTM D2344 standard. At least seven specimens were tested under three-point bending at a crosshead speed of 1 mm min^{-1} until a deflection equal to the thickness of the specimen was achieved. The maximum corresponding force value, F_m, was used to evaluate the ILSS in Equation 1:

$$ILSS = 0.75\frac{F_m}{b \times h} \quad (1)$$

where b is thickness, and h is the width of the specimens. Specimen dimensions of 12.6 mm × 4.2 mm × 2.1 mm according to the span-to-thickness ratio of 4:1, width-to-thickness of 2:1, and overall length-to-thickness of 6:1.

For the flexural strength, a three-point bending test was conducted according to ASTM D790 on composite laminate specimens with the dimensions of 50 × 12.7 × 2.1 mm, and the span-to-depth ratio is fixed to 16:1. The crosshead speed was adopted as 2 mm min^{-1}.

In situ bending test was performed under the optical microscope by using Kammrath Weiss 10 kN bending stage. At least five samples with the dimensions of 10 × 25 × 2.1 mm were tested at a cross-head speed of 1 mm min^{-1}. The span length was set to 18 mm.

Electrical Conductivity: Out-of-plane DC volume electrical conductivity was calculated using the following equation:

$$\sigma = \frac{1}{R}\frac{L}{A} \tag{2}$$

where σ is conductivity (S cm^{-1}), R is measured resistivity (Ω), L is the length of the conductor (cm), and A the cross-sectional area of the sample (cm^2).

To expose the carbon fiber (CF) on the specimen surfaces, the specimens were polished using 320-grit silicon carbide sandpaper, as the manufacturing process left them with uneven resin-rich surfaces. The samples were then bath-ultrasonicated (30 min at a frequency of 40 kHz) in isopropyl alcohol to remove all adhered dust. Copper foil with acrylic-based conductive adhesive (total thickness of 0.04 ± 0.01 mm) was applied to the entire probe contact surfaces of the specimens to create unguarded electrodes. Contact resistance was measured to be 0.6 ± 0.2 Ω. The samples were conditioned overnight at 60 °C under vacuum to remove any absorbed moisture before testing. The samples were tested after cooling down to ambient temperature for 30 min. Before connecting the samples to the leads, the copper electrode surfaces were briefly polished with 800-grit sandpaper to remove any surface corrosion. Direct resistance measurements were recorded using a Fluke 107 multimeter (with a 0.5% error full scale). The samples were connected for a maximum of 1 min to allow readings to stabilize and to minimize errors due to joule heating. Three separate measurements were recorded across three samples (specimens were reconditioned for each measurement).

Thermal Conductivity: Thermal conductivity was measured using the transient plane source method (TPS 2500S) with sensor 7577 (4.002 mm diameter). For each treatment, six square samples of at least 13 mm × 13 mm were prepared using the same procedure as for electrical conductivity specimens. At least four measurements per treatment were recorded by alternating the stacking order. A measurement time of 2 s was used with a heating power of 60 mW. The measurement time and heating power were selected based on the probing depth being less than the sample thickness and the characteristic time between 0.33 and 1 s. The sample temperature change was measured to be with a characteristic time of 0.8–0.9 s. The characteristic time is defined as:

$$\Theta = r^2/k_{axial} \tag{3}$$

where Θ is the characteristic time, r is the sensor radius, and k_{axial} is the calculated axial diffusivity.

Computational Details: Molecular dynamics simulations were used to determine the intermolecular interactions between the nanoparticles, CNC, GNP, and CNT molecules. The surface interaction was designed by considering multilayer graphite as CF substrate (with each side being 1.5 × D, where D is the area of the nanomaterial and epoxy) and was used to evaluate all interactions. The CNC-NM ratios were 2:1, 1:1, with the name of CF-NM1-CNC2-Epoxy and CF-NM2-CNC1-Epoxy (All MD simulations were conducted using COMPASS forcefield, constructed on laboratory observations of interspecies behavior as well as quantum calculations for modeling water, metal, ceramics, and hydrocarbons. The cutoff range was 15 Å.

Data is extracted when an equilibrium state among the optimized structure of the NMs was reached. This was achieved by minimizing the energy level using the SMART algorithm, a combination of the steepest descent, conjugate gradient, and Newton–Raphson methods. NVT ensemble (constant number, volume, temperature) was kept at the 298 K temperature using the Nose thermostat. Reaching the dynamic equilibrium lasted a total analysis time of up to 3000 ps. The interaction energy E_{int} was calculated as follows:

$$E_{int} = E_{complex} - \left(\Sigma E_{fragment}\right) \tag{4}$$

where $E_{complex}$ is the total energy of the interacting system, and $E_{fragment}$ is the energy of the isolated fragment within the complex.[66]

DFT Calculations: The free energy between different pairs of molecules was determined using DFT calculations with a cluster approach to model the surface of the nanoparticles (please see the Supporting Information). Periodic Boundary Condition was applied. GNP was modeled with a unit cell with optimized parameters of $a = b = 14.75$ Å, $\alpha = \beta = 90.0°$, and $\gamma = 120.0°$ constructed to a supercell 6 × 6 × 1 Å. Dmol3 was used on the Perdew–Burke–Ernzerhof (PBE) functional with Grimme's dispersion correction (PBE-D).[67] Optimizations were performed considering the convergence criteria of 2.0×10^{-5} Hartree, 4.0×10^{-3} Hartree Å, and 5.0×10^{-3} Å for energy, maximum force, and displacement, respectively.

The diameter and length of CNT were 9.49 Å, respectively. The a and b parameters rise to 30 Å, which was the same as the c parameter in GNP, to control their Van der Waals interaction with CNC. The role of surface defects was examined in six common defect models. Interactions were evaluated for a CNC particle at the 4 Å vicinity of the NMs, where orbital overlap was possible.

Supporting Information

Supporting Information is available from the Wiley Online Library or from the author.

Acknowledgements

O.K., E.H. contributed equally to this work. This material was based upon work supported by the National Science Foundation, CMMI, Advanced Manufacturing under Grants #1930277, and #2134465. The authors would like to acknowledge that the characterization part of this work was conducted at Texas A & M University Materials Characterization Core Facility (RRID: SCR_022202).

Conflict of Interest

The authors declare no conflict of interest.

Data Availability Statement

The data that support the findings of this study are available on request from the corresponding author. The data are not publicly available due to privacy or ethical restrictions.

Keywords

carbon nanomaterials, cellulose nanocrystals, nano patterning, nanostructured hierarchical composites

Received: January 31, 2023
Revised: May 18, 2023
Published online:

[1] J. Riggs, *Encyclopedia of Polymer Science and Engineering*, Vol. *2*, (Eds.: H.F. Mark, J.I. Kroschwitz), Wiley, New York **1985**.
[2] J. F. Kadla, S. Kubo, R. A. Venditti, R. D. Gilbert, A. L. Compere, W. Griffith, *Carbon* **2002**, *40*, 2913.
[3] M. Perner, S. Algermissen, R. Keimer, H. P. Monner, *Robot Comput Integr Manuf* **2016**, *38*, 82.
[4] D. G. Papageorgiou, Z. Li, M. Liu, I. A. Kinloch, R. J. Young, *Nanoscale* **2020**, *12*, 2228.
[5] Y. Miyano, M. Nakada, *Composites, Part B* **2020**, *191*, 107977.
[6] H. N. Li, J. P. Wang, C. Q. Wu, Y. J. Zhao, J. Xu, X. Liu, W. Q. Zhu, *Composites, Part B* **2020**, *185*, 107774.
[7] N. Geier, J. P. Davim, T. Szalay, *Composites, Part A* **2019**, *125*, 105552.
[8] D. I. Poór, N. Geier, C. Pereszlai, J. Xu, *Composites, Part B* **2021**, *223*, 109155.
[9] S. Hegde, B. S. Shenoy, K. Chethan, *Mater Today Proc* **2019**, *19*, 658.
[10] A. Asadi, M. Miller, R. J. Moon, K. Kalaitzidou, *eXPRESS Polym. Lett.* **2016**, *10*, 587.
[11] O. Kaynan, L. Perez, A. Asadi, presented at *Proc. of the American Society for Composites—Thirty-Sixth Technical Conf. on Composite Materials* September **2021**.
[12] Y. J. Kwon, Y. Kim, H. Jeon, S. Cho, W. Lee, J. U. Lee, *Composites, Part B* **2017**, *122*, 23.
[13] W. Qin, C. Chen, J. Zhou, J. Meng, *Materials* **2020**, *13*, 1457.
[14] O. Kaynan, L. M. Pérez, A. Asadi, *ACS Appl. Nano Mater.* **2022**, *5*, 1284.
[15] H. G. Chae, B. A. Newcomb, P. V. Gulgunje, Y. Liu, K. K. Gupta, M. G. Kamath, K. M. Lyons, S. Ghoshal, C. Pramanik, L. Giannuzzi, K. Şahin, I. Chasiotis, S. Kumar, *Carbon* **2015**, *93*, 81.
[16] B. A. Patterson, H. A. Sodano, *ACS Appl. Mater. Interfaces* **2016**, *8*, 33963.
[17] L.-G. Tang, J. L. Kardos, *Polym. Compos.* **1997**, *18*, 100.
[18] H. Zheng, W. Zhang, B. Li, J. Zhu, C. Wang, G. Song, G. Wu, X. Yang, Y. Huang, L. Ma, *Composites, Part B* **2022**, 109639.
[19] M. He, P. Xu, Y. Zhang, K. Liu, X. Yang, *Chem. Eng. J.* **2020**, *388*, 124255.
[20] T.-M. Liu, Y.-S. Zheng, J. Hu, *J. Appl. Polym. Sci.* **2010**, *118*, 2541.
[21] G. J. Ehlert, Y. Lin, H. A. Sodano, *Carbon* **2011**, *49*, 4246.
[22] M. T. Kim, K. Y. Rhee, J. H. Lee, D. Hui, A. K. T. Lau, *Composites, Part B* **2011**, *42*, 1257.
[23] X. Zhang, T. Sun, Y. Lei, M. Liang, H. Zou, *Composites, Part A* **2021**, *145*, 106372.
[24] R. J. Sager, P. J. Klein, D. C. Lagoudas, Q. Zhang, J. Liu, L. Dai, J. W. Baur, *Compos. Sci. Technol.* **2009**, *69*, 898.
[25] S. Tamrakar, Q. An, E. T. Thostenson, A. N. Rider, B. Z. (G) Haque, J. W. Gillespie, *ACS Appl. Mater. Interfaces* **2016**, *8*, 1501.
[26] R. Sritharan, D. Askari, *Composites, Part B* **2021**, *221*, 108999.
[27] H. Mahmood, L. Vanzetti, M. Bersani, A. Pegoretti, *Composites, Part A* **2018**, *107*, 112.
[28] P.-Y. Hung, K.-T. Lau, B. Fox, N. Hameed, B. Jia, J. H. Lee, *Carbon* **2019**, *152*, 556.
[29] J. P. Johnston, B. Koo, N. Subramanian, A. Chattopadhyay, *Composites, Part B* **2017**, *111*, 27.
[30] A. M. Díez-Pascual, M. A. Gómez-Fatou, F. Ania, A. Flores, *J. Phys. Chem. C* **2012**, *116*, 24193.
[31] W. Qin, F. Vautard, L. T. Drzal, J. Yu, *Composites, Part B* **2015**, *69*, 335.
[32] T. Kamae, L. T. Drzal, *Composites, Part A* **2022**, *160*, 107023.
[33] X. Yao, X. Gao, J. Jiang, C. Xu, C. Deng, J. Wang, *Composites, Part B* **2018**, *132*, 170.
[34] Y. Hu, S. Pang, J. Li, J. Jiang, D. G. Papageorgiou, *Composites, Part B* **2022**, *237*, 109871.
[35] Y. Wu, Z. Wang, L. Xu, H. Wang, S. Peng, L. Zheng, Z. Yang, L. Wu, J.-T. Miao, *Composites, Part A* **2021**, *146*, 106421.
[36] Y. Su, S. Zhang, X. Zhang, Z. Zhao, D. Jing, *Composites, Part A* **2018**, *108*, 89.
[37] H. Zhang, Y. Liu, M. Kuwata, E. Bilotti, T. Peijs, *Composites, Part A* **2015**, *70*, 102.
[38] D.-J. Kwon, J.-Y. Choi, P-S. Shin, K. L. Devries, J.-M. Park, *Adv. Compos. Mater.* **2016**, *25*, 515.
[39] G. Lee, K. D. Ko, Y. C. Yu, J. Lee, W.-R. Yu, J. H. Youk, *Composites, Part A* **2015**, *69*, 132.
[40] J. Xing, G. Zhang, X. Jia, D. Liu, I. Wyman, *ACS Appl. Mater. Interfaces* **2021**, *13*, 4485.
[41] M. Park, W. Cho, G. Lee, S. C. Hong, M.-C. Kim, J. Yoon, N. Ahn, M. Choi, *Small* **2019**, *15*, 1804005.
[42] Y. Zheng, J. Kong, D. Huang, W. Shi, L. Mcmillon-Brown, H. E. Katz, J. Yu, A. D. Taylor, *Nanoscale* **2018**, *10*, 11342.
[43] K. Thorkelsson, P. Bai, T. Xu, *Nano Today* **2015**, *10*, 48.
[44] H. Park, A. Afzali, S.-J. Han, G. S. Tulevski, A. D. Franklin, J. Tersoff, J. B. Hannon, W. Haensch, *Nat. Nanotechnol.* **2012**, *7*, 787.
[45] E. Anaya-Plaza, A. Shaukat, I. Lehtonen, M. A. Kostiainen, *Adv. Healthcare Mater.* **2021**, *10*, 2001162.
[46] X. Guo, J. Su, H. Guo, *Soft Matter* **2012**, *8*, 1010.
[47] D. P. Long, J. L. Lazorcik, R. Shashidhar, *Adv. Mater.* **2004**, *16*, 814.
[48] B. Jia, L. Gao, J. Sun, *Carbon* **2007**, *45*, 1476.
[49] C. J. Murphy, C. J. Orendorff, *Adv. Mater.* **2005**, *17*, 2173.
[50] K. R. Jinkins, J. Chan, R. M. Jacobberger, A. Berson, M. S. Arnold, *Adv. Electron. Mater.* **2019**, *5*, 1800593.
[51] A. Corletto, J. G. Shapter, *ACS Appl. Nano Mater.* **2020**, *3*, 8148.
[52] N. Prochukhan, A. Selkirk, R. Lundy, E. C. Giraud, T. Ghoshal, C. Downing, M. A. Morris, *Langmuir* **2021**, *37*, 1932.
[53] S. Hao, J. Wang, M. Lavorgna, G. Fei, Z. Wang, H. Xia, *ACS Appl. Mater. Interfaces* **2020**, *12*, 968
[54] J. S. Al-Otaibi, Y. S. Mary, R. N. Devi, S. Soman, *J Mol Model* **2020**, *26*, 133633.
[55] A. Hajian, S. B. Lindström, T. Pettersson, M. M. Hamedi, L. Wågberg, *Nano Lett.* **2017**, *17*, 1439.
[56] S. Shariatnia, A. V. Kumar, O. Kaynan, A. Asadi, *ACS Appl. Nano Mater.* **2020**, *3*, 5421.
[57] M. Aramfard, O. Kaynan, E. Hosseini, M. Zakertabrizi, L. M. Pérez, A. Asadi, *Small* **2022**, 2202216.
[58] S. Shariatnia, M. Zakertabrizi, E. Hosseini, K. Song, D. Jarrahbashi, A. Asadi, *Adv. Mater. Technol.* **2023**, *8*, 2201569.
[59] T. Josyula, Z. Wang, A. Askounis, D. Orejon, S. Harish, Y. Takata, P. S. Mahapatra, A. Pattamatta, *Phys Rev E* **2018**, *98*, 052804.
[60] A. Marin, S. Karpitschka, D. Noguera-Marín, M. A. Cabrerizo-Vílchez, M. Rossi, C. J. Kähler, M. A. Rodríguez Valverde, *Phys. Rev Fluids* **2019**, *4*, 041601.
[61] L. Zeng, W. Tao, J. Zhao, Y. Li, R. Li, *Nanotechnol. Rev.* **2022**, *11*, 625.
[62] Y. Ma, Y. Zhao, F. Li, Y. Xu, X. Wei, Y. Chen, J. Wang, H. Jin, *Polym. Compos.* **2021**, *42*, 5574.
[63] N. Ning, M. Wang, G. Zhou, Y. Qiu, Y. Wei, *Composites, Part B* **2022**, *234*, 109749.
[64] T. Khan, M. S. Irfan, M. Ali, Y. Dong, S. Ramakrishna, R. Umer, *Carbon* **2021**, *176*, 602.
[65] S. Shariatnia, A. Asadi, D. Jarrahbashi, *Phys. Fluids* **2021**, *33*, 013314.
[66] E. Hosseini, M. Zakertabrizi, S. Shariati, A. Islam Rajib, E. H. Fini, *Appl. Surf. Sci.* **2021**, *558*, 149954.
[67] E. Hosseini, M. Zakertabrizi, A. Habibnejad Korayem, Z. Zaker, R. Shahsavari, *ACS Nano* **2020**, *14*, 9466.